Author's personal copy

Provided for non-commercial research and educational use.
Not for reproduction, distribution or commercial use.

This article was originally published in Encyclopedia of Interfacial Chemistry, published by Elsevier, and the attached copy is provided by Elsevier for the author's benefit and for the benefit of the author's institution, for non-commercial research and educational use including without limitation use in instruction at your institution, sending it to specific colleagues who you know, and providing a copy to your institution's administrator.

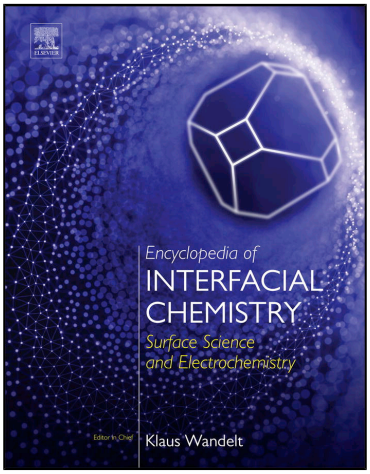

All other uses, reproduction and distribution, including without limitation commercial reprints, selling or licensing copies or access, or posting on open internet sites, your personal or institution's website or repository, are prohibited. For exceptions, permission may be sought for such use through Elsevier's permissions site at:
https://www.elsevier.com/about/our-business/policies/copyright/permissions

From Liu, N.; Zhu, Z.; Noël, J. J.; Shoesmith, D. W. 2018. Corrosion of Nuclear Fuel Inside a Failed Waste Container. In: Wandelt, K., (Ed.) Encyclopedia of Interfacial Chemistry: Surface Science and Electrochemistry, vol. 6, pp 172–182.
ISBN: 9780128097397
Copyright © 2018 Elsevier Inc. All rights reserved.
Elsevier

Author's personal copy

Corrosion of Nuclear Fuel Inside a Failed Waste Container

N Liu, Z Zhu, JJ Noël, and DW Shoesmith, The University of Western Ontario, London, ON, Canada

© 2018 Elsevier Inc. All rights reserved.

Nomenclature

at%	Atomic percentage
CANDU	Canada Deuterium Uranium
CS-AFM	Current-sensing atomic force microscopy
E_{CORR}	Corrosion potential
EDX	Energy-dispersive X-ray spectroscopy
j_k	Kinetic current density
LWR	Light water reactor
O_I	Interstitial oxygen
O_V	Oxygen vacancy
RE	Rare earth
SCE	Saturated calomel electrode
SECM	Scanning electrochemical microscopy
SIMFUEL	UO_2 doped with nonradioactive elements
wt%	Weight percentage
XPS	X-ray photoelectron spectroscopy

Introduction

The direct disposal of spent nuclear fuel in deep geologic repositories has been under investigation internationally for over 30 years. Various geologic formations are being, or have been, studied. The spent nuclear fuel would be encapsulated and sealed inside a metallic container, most likely fabricated from carbon steel, possibly with an outer copper shell or deposited coating, and emplaced in bore holes or deposition tunnels. The space between the container and the borehole/tunnel wall would then be backfilled with sealing materials such as clay. Such a repository can provide acceptable assurance for the long-term containment and isolation of the fuel. However, since regulatory radioactivity release limits require containment for many thousands of years, it is essential to consider the consequences of container failure leading to exposure of the fuel to groundwater. Since the spent fuel contains the radioactive fission and activation products, its behavior in contact with ground water provides the critical radioactivity source term in any assessment of repository safety.

The universally common form of nuclear fuel is stoichiometric uranium dioxide (UO_2) fabricated as high-density cylindrical ceramic pellets (94%–97% of theoretical density) approximately 1 cm in diameter, contained within sheathing made of Zircaloy, a corrosion-resistant Zr alloy. The majority of the fuel used in light water reactors is enriched (to 1%–5%) in the fissile isotope ^{235}U, while fuel used in Canadian (CANDU: CANada Deuterium Uranium) reactors is un-enriched (0.712% ^{235}U).

In reactor, irradiation leads to the formation of a wide range of radionuclides as a result of fission, neutron capture, and activation events. The fuel also undergoes a number of microstructural and chemical changes. The initially fine-grained interlocking

Author's personal copy

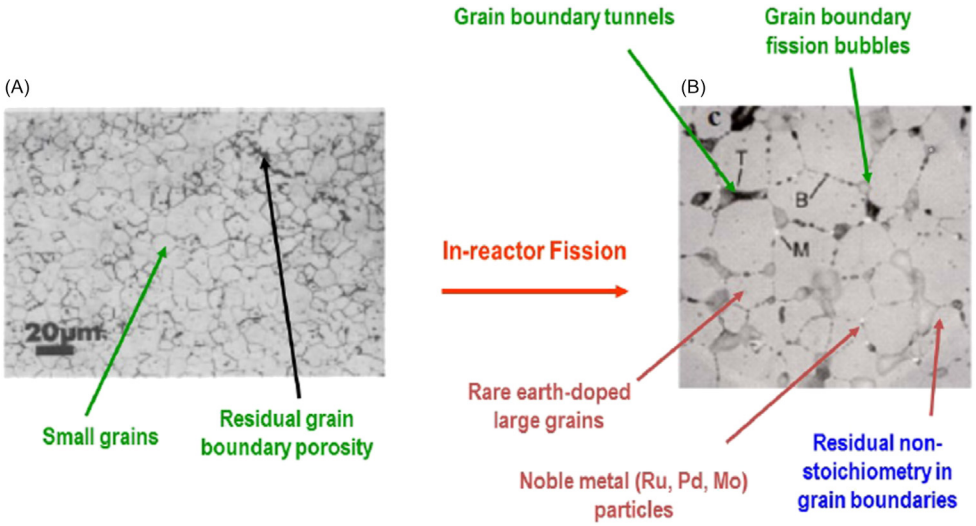

Fig. 1 Scanning electron microscopy images of UO_2 fuel: (A) un-irradiated UO2; and (B) irradiated UO_2 fuel. In (A) two key features of un-irradiated fuel are noted. In (B) features which cannot be simulated in SIMFUELs are noted in *green*; features which can be simulated in SIMFUELs are noted in *red*; features simulated in other fuel specimens are noted in *blue*.

microstructure, containing some residual porosity from the sintering process, undergoes grain growth and the formation of gas bubbles, which lead to the development of gas tunnels along grain boundaries. The chemical composition and microstructure of spent fuels have been extensively studied. Based on these analyses, the key changes likely to influence the reactivity of the fuel under disposal conditions are summarized in Fig. 1.

A number of these features can be simulated in un-irradiated fuel analogs: (1) rare earth (RE^{III}) doping of the UO_2 fluorite matrix; (2) the presence of noble metal particles; and (3) nonstoichiometry, though not necessarily located in grain boundaries. The physical changes, such as the introduction of grain boundary tunnels and fission bubbles are more difficult to simulate.

Those radionuclides that have escaped the fuel matrix and are available for rapid release on contact with groundwater have been determined and their leaching behavior intensively studied. However, the release of ~90% of radionuclides will be governed by the corrosion/dissolution of the UO_2 matrix. The rate of this process will be related to, but not necessarily directly proportional to, the solubility of U in the groundwater. While groundwater entering a failed container will be anoxic, its radiolysis, due to radioactive decay processes within the fuel, will produce a variety of chemical species, including oxidants. Since U is considerably more soluble as U^{VI} than as U^{IV}, reaction of the fuel with radiolytic oxidants will lead to corrosion and radionuclide release, Fig. 2.

The rate of corrosion will depend on the redox conditions within the container and hence on the radiation dose rate at the fuel surface, which will be dominated in the long term by the alpha-dose rate, Fig. 2. Since the production of radiolytic oxidants will decrease with time, redox conditions will evolve from oxidizing to anoxic. As illustrated in Fig. 3, two corrosion fronts will exist within the container, one on the fuel surface driven by radiolytic oxidants and a second on the inner surface of the carbon steel container, sustained by the reaction with H_2O to produce Fe^{2+} and H_2. In this illustration, H_2O_2 is taken to be the primary oxidant, although the production of O_2 via H_2O_2 decomposition would produce an additional oxidant. The key radiolytic and corrosion products are illustrated in Fig. 3. Since the corrosion potentials (E_{CORR}) of the two surfaces will be very different, the products

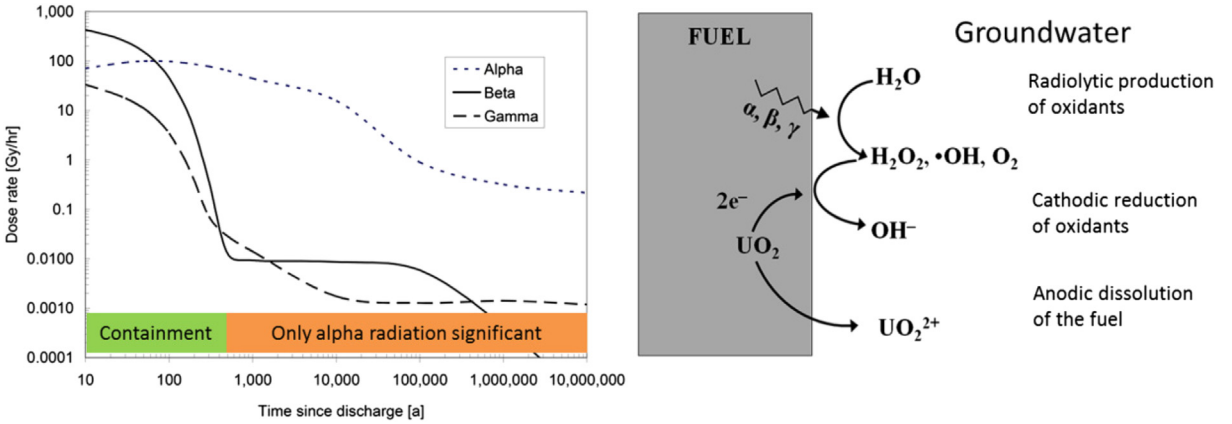

Fig. 2 Alpha, beta, and gamma radiation dose rates as a function of time are shown on the *left* (CANDU fuel bundle with a 220 MWh/kgU burnup). The scheme on the *right* illustrates the radiolytic corrosion process leading to radionuclide release.

Author's personal copy

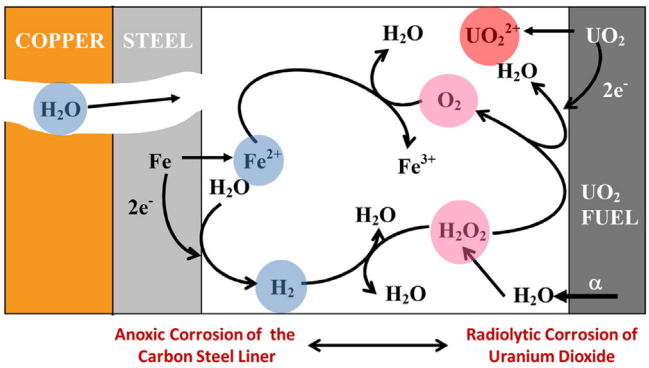

Fig. 3 The key chemical and electrochemical reactions anticipated inside a failed, groundwater flooded waste container. The highlighted species are those whose production and interactions will control the redox conditions at the fuel surface.

of radiolysis (H_2O_2, O_2) will be unstable in the presence of the steel corrosion products, Fe^{2+} and H_2, which will regulate the redox conditions at the fuel surface.

Based on sensitivity calculations using a mixed potential electrochemical model developed to describe reactions occurring within a failed container, the following features were found to dominate fuel corrosion: (1) the reactivity of the fuel; (2) the reduction kinetics of H_2O_2 or O_2 produced by H_2O_2 decomposition; and (3) the scavenging of radiolytic oxidants by steel corrosion products.

Reactivity of the Fuel

Composition of the UO_2 Surface as a Function of Redox Conditions

The composition of the UO_2 surface has been mapped as a function of potential using electrochemical methods and X-ray photoelectron spectroscopy (XPS), Fig. 4.

Significant oxidation occurs at potentials >-0.4 V (vs. SCE), consistent with thermodynamics. All three oxidation states (U^{IV}, U^{V}, and U^{VI}) can be detected with the extent of oxidation proceeding through the compositional sequence indicated on the figure. Prior to conversion to U^{VI}, the top few nanometers of the surface are oxidized to $U^{IV}_{1-2x}U^{V}_{2x}O_{2+x}$, with x varying with potential, and oxygen ions (O^{II}) being injected into the fluorite lattice to maintain charge neutrality. This thin layer possesses catalytic properties important in determining corrosion kinetics. Whether or not the surface is catalytic depends on the value of x. Using Raman spectroscopy and electrochemical/corrosion measurements, it has been shown that the surface is catalytic while interstitial oxygen ions (O_I) are randomly distributed and the fluorite matrix maintained, but catalytic activity is lost once tetragonal distortions initiate the formation of cuboctahedral clusters, a transition which appears to occur around a composition of $U^{IV}_{0.7}U^{V}_{0.3}O_{2.15}$ (see below).

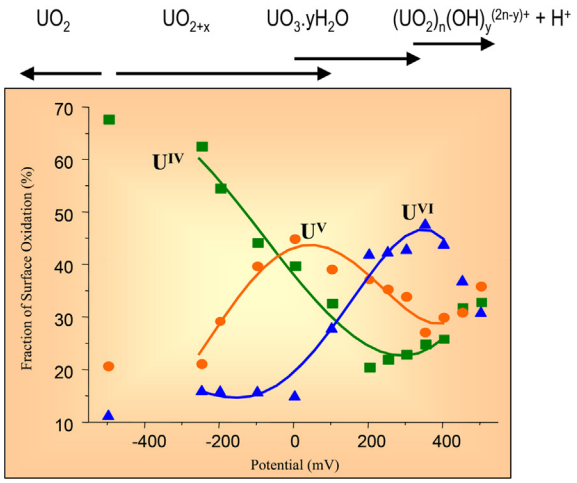

Fig. 4 The fractions of the oxidation states of uranium in the surface of SIMFUEL (1.5 at%) obtained by XPS after electrochemical oxidation for 1 h at each potential in 0.1 mol L^{-1} NaCl solution (pH = 9.5). For potentials >350 mV, the solution at the electrode surface becomes acidic due to the hydrolysis of UO_2^{2+}.

Author's personal copy

At higher potentials, oxidation yields the more soluble U^{VI}, when dissolution as $U^{VI}O_2^{2+}$ and its redeposition as $U^{VI}O_3\bullet yH_2O$ can occur. In the presence of HCO_3^-/CO_3^{2-}, anticipated groundwater anions, complexation of $U^{VI}O_2^{2+}$ can accelerate dissolution by preventing the deposition of $U^{VI}O_3\bullet yH_2O$ and thinning the $U^{IV}_{1-2x}U^{V}_{2x}O_{2+x}$ surface layer. The details of the dissolution reaction in HCO_3^-/CO_3^{2-} have been elucidated using electrochemical impedance spectroscopy, with the reaction shown to proceed via adsorbed U^V and U^{VI} intermediates,

$$U^{IV}O_2 + HCO_3^- \rightarrow U^{V}O_2(HCO_3)_{ads} + e^- \quad (1)$$

$$U^{V}O_2(HCO_3)_{ads} + OH^- \rightarrow \left(U^{VI}O_2CO_3\right)_{ads} + H_2O + e^- \quad (2)$$

$$\left(U^{VI}O_2CO_3\right)_{ads} + HCO_3^- \rightarrow U^{VI}O_2(CO_3)_2^{2-} + H^+ \quad (3)$$

Other groundwater species, such as Ca^{2+} and silicate, can stabilize U^{VI} deposits on the electrode surface leading to the suppression of the corrosion rate.

The Influence of RE^{III} Doping on Reactivity

Considerable experimental evidence exists to show that doping of the $U^{IV}O_2$ matrix by fission products (in particular RE^{III}) and actinides–lanthanides influences the kinetics of air oxidation of the fuel. Electrochemical studies show that RE^{III} doping similarly influences the anodic reactivity in aqueous solutions. These latter studies, combined with XPS analyses, confirm that the overall influence of potential on anodic behavior is similar to that observed on undoped $U^{IV}O_2$, with doping suppressing both matrix oxidation ($U^{IV}O_2 \rightarrow U^{IV}_{1-2x}U^{V}_{2x}O_{2+x}$) and the subsequent oxidation to U^{VI} ($U^{IV}_{1-2x}U^{V}_{2x}O_{2+x} \rightarrow U^{VI}O_2^{2+}$). The second step is more influenced than the first, consistent with the influence of RE^{III} doping on air oxidation, which also proceeds in two stages ($UO_2 \rightarrow U_3O_7/U_4O_9 \rightarrow U_3O_8$). Raman spectroscopy shows the $U^{IV}O_2$ structure becomes increasingly dominated by the presence of RE^{III}-O_V clusters (O_V: oxygen vacancy), limiting the number of O_V available to accommodate the O_I injection required for oxidation.

Comparison of the reactivity of $UO_{2.002}$, Gd-doped (6 wt%), Dy-doped (13 wt%) UO_2, and SIMFUEL (1.5 at%: UO_2 doped with nonradioactive elements including rare earths (Ba, Ce, La, Sr, Mo, Y, Zr, RH, Pd, Ru, and Nd) to replicate the chemical effects of in-reactor irradiation) confirms that both stages of oxidation are suppressed and that once anodic dissolution commences the order of reactivity is

$$UO_{2.002} > \text{SIMFUEL} > \text{Gd} - \text{doped } UO_2 > \text{Dy} - \text{doped } UO_2$$

as shown in Fig. 5.

For $UO_{2.002}$, the onset of dissolution at sub-thermodynamic potentials can be attributed to the enhanced reactivity on nonstoichiometric areas (see below), as demonstrated by current-sensing atomic force microscopy (CS-AFM). XPS and Raman spectroscopy demonstrate that dissolution of doped specimens requires sufficient surface oxidation to cause tetragonal lattice distortions (around $U^{IV}_{0.7}U^{V}_{0.3}O_{2.15}$) leading to defect clustering. Clustering leads to enhanced diffusion of O_I to deeper locations and the destabilization of the fluorite lattice.

Electrochemical studies of a series of Gd-doped specimens ($U^{IV}_{1-y}Gd^{III}_{y}$)O_2 ($0 \le y \le 0.1$) show that the reactivity increases only slightly up to $y = 0.05$ before decreasing more obviously at higher doping levels ($y > 0.05$), Fig. 6.

Based on X-ray diffraction and Raman spectroscopic measurements, this is attributed to an increase in the number of O_V, accounting for the slight acceleration at low-doping levels, and the reduction of O_V by formation of RE^{III}–O_V clusters accompanied

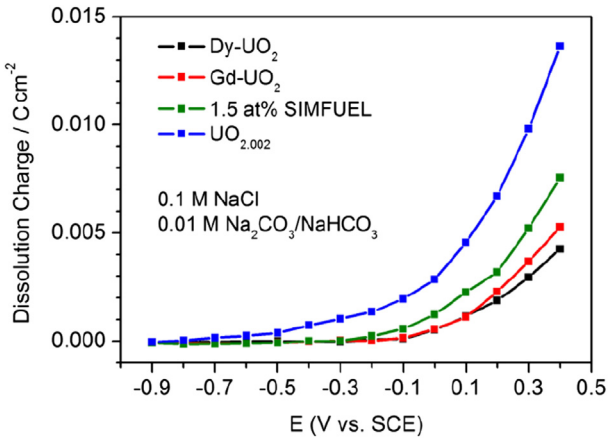

Fig. 5 Dissolution charges measured electrochemically for four different UO_2 specimens.

Author's personal copy

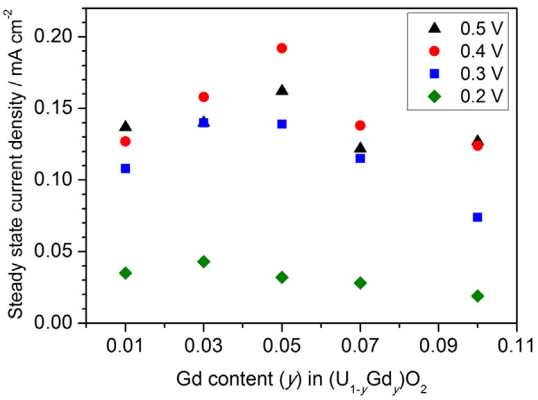

Fig. 6 Steady-state current densities measured on $(U^{IV}_{1-y}Gd^{III}_{y})O_2$ electrodes as a function of Gd content measured after anodic oxidation at different potentials (vs. SCE) for 1 h in 0.1 mol L^{-1} NaCl containing 0.05 mol L^{-1} $NaHCO_3/Na_2CO_3$.

by a lattice contraction, which suppresses reactivity at the high-doping levels. A similar minor effect of lattice doping is observed for SIMFUELs (1.5, 3.0, 6.0 at%).

The Influence of Nonstoichiometry on Reactivity

As suggested by the early onset of anodic dissolution, Fig. 5, the influence of nonstoichiometry on the electrochemistry and corrosion of UO_2 is more marked than that of RE^{III} doping. The availability of octahedral holes in the fluorite structure allows UO_2 to accommodate large amounts of O_I to form hyperstoichiometric $U^{IV}_{1-2x}U^{V}_{2x}O_{2+x}$, the energy of O_I formation being negative. The influence of nonstoichiometry on the structure of UO_2 is demonstrated the characterization of specimens with nominal stoichiometry ranging from $UO_{2.002}$ to $UO_{2.1}$ but comprising grains with compositions varying from $\sim UO_{2.001}$ to $\sim UO_{2.3}$. Fig. 7 shows the influence of increasing nonstoichiometry on the lattice structure, determined by micro Raman analyses on grains with different compositions in the $UO_{2.1}$ specimen.

Close to stoichiometry, the spectrum is dominated by the fundamental O–U stretch (445 cm^{-1}) and a broader peak at 1150 cm^{-1} (not shown) is attributed to an overtone of the L–O phonon band at 575 cm^{-1}. As the degree of nonstoichiometry

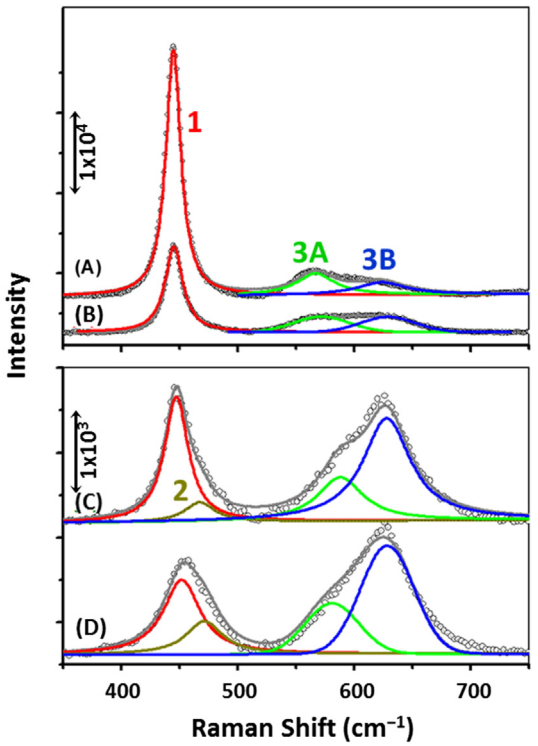

Fig. 7 Sections of Raman spectra recorded on a $U^{IV}_{1-2x}U^{V}_{2x}O_{2+x}$ specimens with individual grains with different stoichiometries: (A) $UO_{2.01}$; (B) $UO_{2.15}$; (C) $UO_{2.22}$; and (D) $UO_{2.31}$.

Author's personal copy

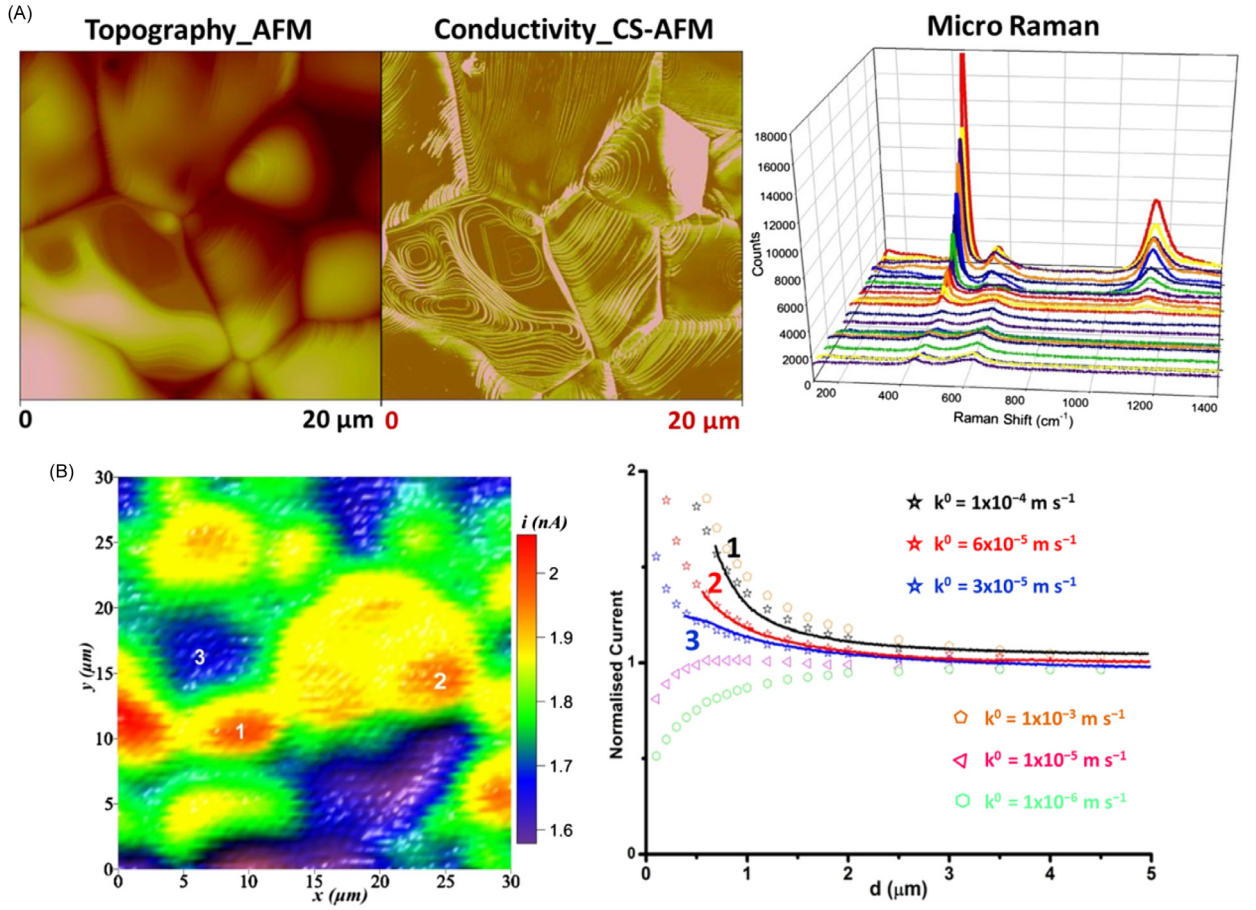

Fig. 8 (A) AFM, CS-AFM, and Raman spot analyses recorded on a specimen with the nominal stoichiometry of $UO_{2.1}$. Raman spectra were recorded at a series of locations and arranged according to the intensity of the band at 445 cm^{-1}. The CS-AFM image is color-coded according to standard AFM practice with conducting regions shown as *bright* and regions of lower conductivity as *dark areas*. (B) An SECM map (30 µm by 30 µm) and probe approach curves recorded on an electrode with a nominal stoichiometry of $UO_{2.1}$ at E_{CORR} in 0.1 mol L^{-1} NaCl (pH 9.5). The current range is indicated in the *bar* on the image. The probe approach curves recorded at the numbered locations are superimposed on a series of theoretical curves calculated for various values of the rate constant for the cathodic reaction on the corroding UO_{2+x} substrate surface.

is increased, the loss of intensity in the 445 cm^{-1} (peak 1) and development of a shoulder around 470 cm^{-1} (peak 2) indicate tetragonal distortions in the fluorite lattice. Simultaneously, the relative importance of the broad multicomponent band (500–700 cm^{-1} (peak 3)) increases. The decreasing importance of the L–O phonon (peak 3A) relative to peak 3B at 640 cm^{-1}, indicates these lattice distortions are accompanied by the formation of cuboctahedral clusters, the latter peak being attributable to this feature. These lattice changes occur around a composition of $U^{IV}_{0.7}U^{V}_{0.7}O_{2.15}$ and lead to extensive anodic reactivity.

A relationship between these changes and an increase in corrosion rate can be demonstrated by a combination of energy dispersive X-ray analyses, micro Raman spectroscopy to characterize surface structure, CS-AFM to relate the degree of nonstoichiometry to the electrical conductivity, and scanning electrochemical microscopy (SECM), using the redox mediator ferrocenemethanol as the oxidant. Fig. 8 shows a series of such measurements on the nominally $UO_{2.1}$ specimen. Similar measurements on specimens with various stoichiometries ($UO_{2.002}$, $UO_{2.011}$, $UO_{2.05}$, and $UO_{2.1}$) show that, as nonstoichiometry increases up to $UO_{2.3}$, the corrosion rate increases by $\sim 10^3$.

Oxidant Reduction Reactions

If container failure occurs while γ/β radiation fields are significant (Fig. 2), fuel corrosion would be driven by both radical and molecular oxidants. However, while radical oxidants (e.g., OH●) are highly reactive, their steady-state concentrations would be low, and fuel corrosion would be predominantly driven by H_2O_2, which will be present in substantially larger amounts. If container failure is delayed until only α-radiolysis is a significant source of oxidants (Fig. 2), H_2O_2 would be the only meaningful oxidant unless it decomposes to O_2, which reacts ~200 times more slowly with the fuel surface than does H_2O_2.

$$2H_2O_2 \rightarrow O_2 + H_2O \quad (4)$$

Author's personal copy

Kinetics of Oxygen Reduction

The cathodic reduction of O_2 is notoriously slow due to the need to break the O–O bond. On UO_2, the kinetics are accelerated by oxidizing the surface to $U^{IV}_{1-2x}U^{V}_{2x}O_{2+x}$ in aerated solutions indicating catalysis by donor–acceptor sites, that is, adjacent U^{IV}–U^{V} atoms, which relay electrons. The reaction is first order with respect to $[O_2]$ and thought to initiate by O_2 adsorption under Langmuir isotherm conditions involving the interaction of the π and/or sp^2 orbitals of O_2 with partially filled U5f orbitals present in $U^{IV}_{1-2x}U^{V}_{2x}O_{2+x}$. The reaction sequence is illustrated in Fig. 9.

For highly nonstoichiometric specimens, O_2 reduction currents are suppressed, with a square root dependence on $[O_2]$ and exhibit large Tafel slopes, suggesting the rate determining first electron transfer is coupled with O_2 adsorption under Temkin isotherm conditions. The tendency of O_I to form defect clusters may also deactivate some donor–acceptor sites for O_2 reduction by isolating them from the matrix conductive network.

The O_2 reduction current is also decreased by competition for U^{V} surface locations in HCO_3^-/CO_3^{2-} solutions. Since the O_2 reaction order and the Tafel slopes are apparently unaffected by the presence of HCO_3^-/CO_3^{2-}, the overall reduction mechanism appears to be unaltered, although ring-disc experiments show that H_2O_2 is released to solution, indicating its rapid desorption due to displacement from the donor–acceptor sites by HCO_3^-/CO_3^{2-}.

Both RE^{III} doping and the presence of noble metal particles influence the kinetics of O_2 reduction, Fig. 10.

Fission product doping (with RE^{III}, the major influence) has only a marginal effect on the kinetics, but an increase in number and size of noble metal particles present in SIMFUELs (over the simulated burnup range 1.5–6 at%) systematically increases the reduction rate of O_2. This is not surprising since these particles contain the noble metals Ru, Rh, and Pd, all of which are known to catalyze this reaction. As a consequence, O_2 reduction in support of fuel corrosion inside a failed container would occur preferentially on these particles.

Kinetics of Hydrogen Peroxide Reduction

The kinetics of H_2O_2 reduction are faster (200 times) than those of O_2. This higher rate is attributed to the ability of H_2O_2 to create U^{IV}–U^{V} donor–acceptor sites rather than relying on their pre-existence, as is the case for O_2 reduction. Under cathodic polarization, reduction involves chemical oxidation of the UO_2, that is, the creation of U^{IV}–U^{V} sites

$$2U^{IV} + H_2O_2 \rightarrow 2U^{V} + 2OH^- \tag{5}$$

followed by their electrochemical destruction,

$$2U^{V} + 2e^- \rightarrow 2U^{IV} \tag{6}$$

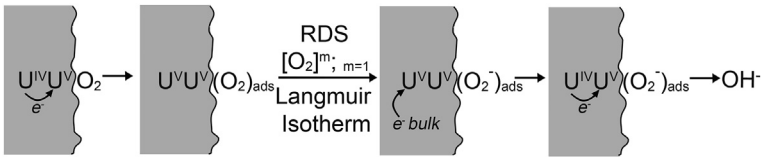

Fig. 9 Reduction of O_2 at donor–acceptor sites on a UO_2 surface.

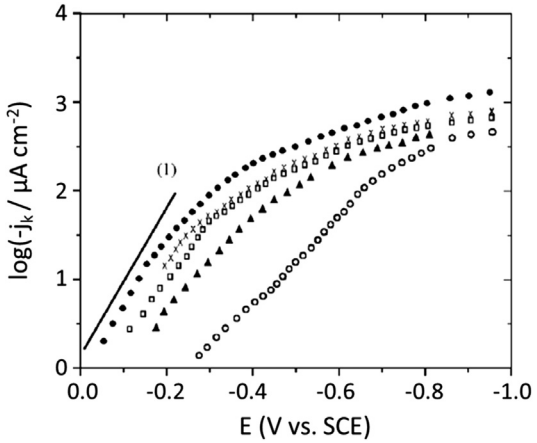

Fig. 10 O_2 reduction currents recorded on various SIMFUEL electrodes in an aerated 0.1 mol L^{-1} NaCl (pH = 9.5) solution: (*o*) SIMFUEL with no noble metal particles; (*triangles*) 1.5 at% SIMFUEL; (*open square*) 3 at% SIMFUEL; (•) 6 at% SIMFUEL; and (*x*) 3 at% SIMFUEL with noble metal particles but no fission products. The line (1) indicates a Tafel slope of 90 mV $decade^{-1}$.

Author's personal copy

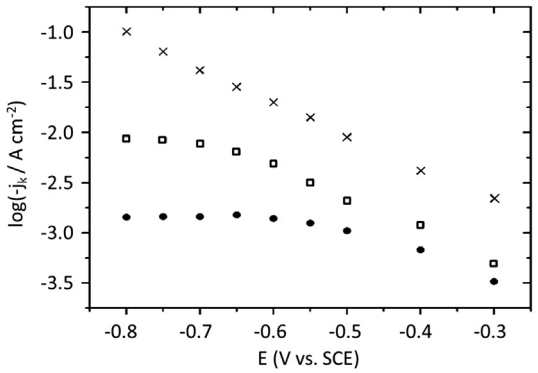

Fig. 11 Tafel plots (transport corrected) recorded on SIMFUEL (no noble metal particles) in 0.1 mol L^{-1} NaCl (pH = 9.7) containing various [H_2O_2]; (*full circle*) 1.3×10^{-4} mol L^{-1}; (*open square*) 4.0×10^{-4} mol L^{-1}; and (*x*) 4.3×10^{-3} mol L^{-1}.

This leads to large Tafel slopes (200–400 mV^{-1}) and fractional reaction orders as a consequence of the potential-dependent surface coverage by active sites. Since the first reaction is dependent on [H_2O_2] and the second on applied potential, the rate controlling reaction changes from electrochemical control at high [H_2O_2], when the initial chemical reaction is fast, to chemical control when the [H_2O_2] is lower and the applied potential sufficiently negative. This transition is illustrated in Fig. 11 for data recorded on a SIMFUEL without noble metal particles.

As for O_2, H_2O_2 reduction could be catalyzed on a RE^{III}-doped surface and on noble metal particles. However, electrochemical studies detect no discernible influence of RE^{III} doping and only a minor influence of noble metal particles. Thus, at the low burnup achieved in spent CANDU fuel (~1.5 at%), no significant influence of noble metal particles on H_2O_2 reduction in support of corrosion would be anticipated. This is a direct consequence of the ability of H_2O_2 to create U^{IV}–U^{V} states, making the kinetics of reduction on the UO_2 surface and on noble metal particles only marginally different.

Under corrosion conditions, the behavior of H_2O_2 is complicated since it can both drive corrosion and decompose. At sufficiently high [H_2O_2] in neutral to alkaline conditions, surface oxidation is found to be rapid, with the potentially catalytic $U^{IV}_{1-2x}U^{V}_{2x}O_{2+x}$ becoming covered by an insulating $U^{VI}O_3 \bullet yH_2O$ layer, and both UO_2 corrosion and H_2O_2 decomposition are limited by the chemical dissolution of U^{VI} species.

Since the dissolution of U^{VI} is accelerated by complexation with HCO_3^-/CO_3^{2-}, both reactions are revived when HCO_3^-/CO_3^{2-} is present. The overall corrosion reaction in HCO_3^-/CO_3^{2-} solutions is complicated since the anodic and cathodic reactions appear to be convoluted. UV–vis spectrophotometric evidence suggesting dissolution is accelerated by the formation of a soluble uranylperoxocarbonate, $U^{VI}O_2(O_2)_x(CO_3)_y^{2-2x-2y}$, and EIS evidence indicating a similar, but ill-defined, surface intermediate may catalyze the cathodic reaction. In addition, H_2O_2 is found to be unstable in HCO_3^-/CO_3^{2-} solutions.

$$H_2O_2 + CO_3^{2-} \rightarrow CO_4^{2-} + H_2O \tag{7}$$

$$H_2O_2 + CO_4^{2-} \rightarrow CO_3^{2-} + H_2O + O_2 \tag{8}$$

H_2O_2 Decomposition

Early studies demonstrate that not all the H_2O_2 consumed in UO_2 dissolution experiments can be accounted for, suggesting H_2O_2 decomposition. Many studies at high [H_2O_2] ($>10^{-4}$ mol L^{-1}) in solutions containing no HCO_3^-/CO_3^{2-} are complicated by corrosion product deposition. When HCO_3^-/CO_3^{2-} is present and dissolution unimpeded by deposits, ~80% of the H_2O_2 is consumed by decomposition. A combination of experimental and density functional theory investigations show decomposition proceeds via a mechanism involving OH● radicals. Electrochemical studies indicate that the reaction is catalyzed by U^{IV}/U^{V} surface states on UO_2, that is, on the catalytic $U^{IV}_{1-2x}U^{V}_{2x}O_{2+x}$ layer, consistent with recent observations that show H_2O_2 maintains a low E_{CORR} (−0.35 V), independent of [H_2O_2] ($10^{-8}-10^{-5}$ mol L^{-1}), as would be expected if decomposition is poising the potential. Recent electrochemical studies demonstrate that decomposition does occur on a $U^{IV}_{1-2x}U^{V}_{2x}O_{2+x}$ surface, XPS analyses showing that preoxidation of stoichiometric UO_2 accelerates the decomposition reaction.

Monitoring the production of OH● in experiments on UO_2, doped UO_2 and SIMFUEL, demonstrates that the decomposition rate is virtually independent of matrix doping. Comparison of the H_2O_2 consumption rate to the U^{VI} dissolution rate shows surface-catalyzed decomposition is the major reaction pathway, not H_2O_2-promoted UO_2 corrosion. The dissolution yield on UO_2 is 14% compared to only 0.2% on SIMFUEL, consistent with electrochemical observations that the UO_2 lattice is stabilized by RE^{III}-doping.

Scavenging Radiolytic Oxidants

As illustrated in Fig. 3, steel corrosion products (Fe^{2+}, H_2) will act as redox scavengers inside a failed container.

Author's personal copy

The Influence of Ferrous Ions

Extensive studies of the influence of Fe and Fe corrosion products on fuel corrosion show that both the corrosion and radionuclide release rates are suppressed. Since there will be no contact between the steel and the fuel inside a container, the dominant scavenging reaction involving Fe^{2+} will be either the Fenton reaction for H_2O_2,

$$Fe^{2+} + H_2O_2 \rightarrow Fe^{3+} + OH\cdot + OH^- \quad (9)$$

$$Fe^{2+} + OH\cdot \rightarrow Fe^{3+} + OH^- \quad (10)$$

or oxidation by O_2,

$$O_2 + 4Fe^{2+} + 2H_2O \rightarrow 4Fe^{3+} + 4OH^- \quad (11)$$

a reaction known to regulate redox conditions in natural waters.

Since the influences of Fe^{2+} and H_2 cannot be separated in experiments with Fe, more direct attempts are required to determine the influence of Fe^{2+} on fuel corrosion, both experimentally and via model calculations. These measurements and calculations show the effectiveness of the Fenton reaction in suppressing fuel corrosion depends on the groundwater composition, which determines whether or not corrosion product deposits are present. When HCO_3^-/CO_3^{2-} is not present, Fe^{2+} is an efficient H_2O_2 scavenger, fuel corrosion rates being reduced by a factor of >40. When products of UO_2 are present, only a minor influence is calculated, the corrosion products acting as a diffusion barrier limiting the access of Fe^{2+} to the location at which H_2O_2 is radiolytically produced. A two-dimensional model accounting for corrosion processes in fuel fractures also shows the effectiveness of Fe^{2+} as a scavenger is limited by its transport to the base of fractures.

The Influence of Hydrogen

The measured steel corrosion rates under simulated granitic conditions are in the range of 0.05–0.1 μm $year^{-1}$. In sealed repositories, this would lead to H_2 pressures >5 MPa, and dissolved concentrations in the 10–100 mmol L^{-1} range. Suppression of fuel corrosion and radionuclide release in the presence of H_2 is consistently observed, well documented, and reviewed. A number of mechanisms can be either demonstrated or proposed, all of which involve activation of H_2 to produce the strongly reducing H● radical, which can scavenge radiolytic oxidants and, hence, suppress fuel corrosion.

Electrochemical studies on SIMFUELs with different levels of simulated burnup show that the activation of H_2 occurs on noble metal particles. That this occurs is not surprising since noble metals are well-known catalysts for the $H_2/H\bullet/H^+$ reaction, with exchange currents in the range of 10^{-4}–10^{-3} A cm^{-2}. Even for small $[H_2]$, E_{CORR} decreases as the number and size of noble metal particles increases, eventually reaching the thermodynamic threshold for UO_2 oxidation (Fig. 12A). XPS analyses confirm that the extent of oxidation of the UO_2 surface is decreased (Fig. 12B).

For higher $[H_2]$, E_{CORR} is decreased to approximately -0.7 V, which is well below the threshold for oxidation, as illustrated in Fig. 13, This can be attributed to the reversible dissociation of H_2 (to H● radicals) on the particles, which act as galvanically coupled anodes protecting the fuel from oxidation. The activation of H_2 on noble metal particles can also consume H_2O_2 by catalyzing its

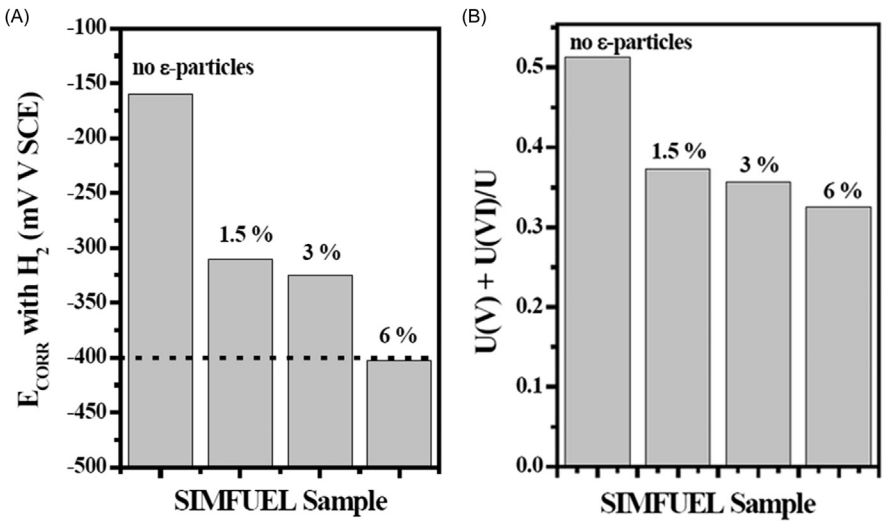

Fig. 12 (A) The influence of the increasing number and size of noble metal particles in SIMFUELs (at%) on E_{CORR} in H_2-purged 0.1 mol L^{-1} KCl. (B) The degree of oxidation of SIMFUEL surfaces after exposure at E_{CORR} in Figure (A).

Author's personal copy

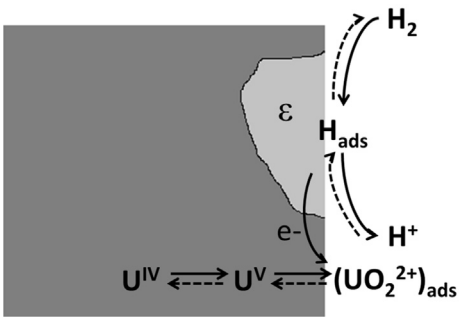

Fig. 13 Illustration showing H_2 oxidation on noble metal (ε) particles galvanically coupled to the UO_2 matrix and inhibiting its oxidation.

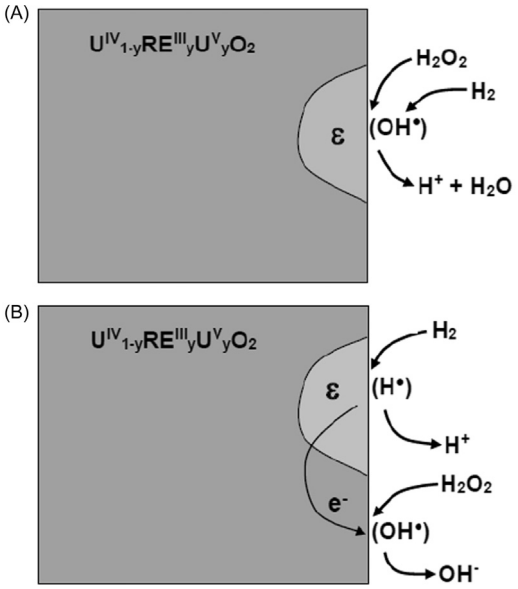

Fig. 14 Schematic illustration of the possible reaction pathways for the consumption of H_2O_2 by reaction with H_2 on a SIMFUEL surface: (A) on noble metal (ε) particles; and (B) by H_2 oxidation on noble metal particles coupled to H_2O_2 reduction on the galvanically coupled oxide surface.

reduction either via direct reaction on the particles, Fig. 14A, or by galvanic coupling H_2 oxidation on the particles with H_2O_2 reduction on the fuel surface, Fig. 14B.

These conclusions are verified by measurements on spent fuels, with a decrease in fuel corrosion rate of $>10^4$ (compared to rates under oxidizing conditions) being achieved in H_2-purged experiments ($[H_2]=0.8$ mmol L^{-1}). Results on α-doped UO_2, UO_2 specimens in close proximity to α-sources, and UO_2 in the presence of γ-radiation also confirm that H_2 suppressed fuel corrosion in the absence of noble metal particles. Both forms of radiation appear able to activate H_2 (i.e., produce H●) on UO_2 surfaces, which then consumes the OH● radicals, produced by dissociation of H_2O_2, to produce H_2O. The mechanism by which this occurs is uncertain, although there is electrochemical evidence to indicate H● can directly reduce U^V states in the surface region of $U^{IV}_{1-2x}U^{V}_{2x}O_{2+x}$.

See also: Corrosion in Oil and Chemical Industry; Corrosion in Pressurized Water; Tribocorrosion.

Further Reading

Broczkowski, M. E.; Zagidulin, D.; Shoesmith, D. W. The Role of Dissolved Hydrogen on the Corrosion/Dissolution of Spent Nuclear Fuel. In Wai, C. M., Mincher, B. J., Eds.;, Vol. 1046; *Proceedings of American Chemical Society Symposium, Nuclear Energy and the Environment*; 2010; pp 349–380. Chapter 26.

Carbol, P.; Cobos-Sabate, J.; Glatz, J.-P.; Ronchi, C.; Rondinella, V.; Wegen, D. H.; Wiss, T.; Loida, A.; Metz, V.; Kienzler, B.; Spahiu, K.; Grambow, B.; Quinones, J.; Martinez Esparza Valiente, A. *The Effect of Dissolved Hydrogen on the Dissolution of ^{233}U-Doped UO_2(s), High Burn-Up Spent Fuel and MOX Fuel Technical Report TR-05-09*, Swedish Nuclear Fuel and Waste Management Company: Stockholm, 2005.

Ekeroth, E.; Roth, O.; Jonsson, M. The Relative Impact of Radiolysis Products in Radiation-Induced Oxidative Dissolution of UO_2. *J. Nucl. Mater.* **2006,** *355,* 38–46.

Author's personal copy

Eriksen, T. E.; Shoesmith, D. W.; Jonsson, M. Radiation Induced Dissolution of UO_2-Based Nuclear Fuel—A Critical Review of Predictive Modelling Approaches. *J. Nucl. Mater.* **2012,** *420,* 409–423.

Grenthe, I.; Fuger, J.; Konings, R. J. M.; Lemire, R. J.; Muller, A. B.; Nguyen-Trung Cregu, C.; Wanner, H. Chemical Thermodynamics of Uranium. In *OECD Nuclear Energy Agency, Data Bank;* Wanner, H., Forest, I., Eds., North Holland Elsevier Science: Amsterdam, 1992.

He, H.; Broczkowski, M.; O'Neil, K.; Ofori, D.; Semenikhin, O.; Shoesmith, D. W. Corrosion of Nuclear Fuel (UO_2) Inside a Failed Nuclear Waste Container. In *Technical Report TR-2012-09*, Nuclear Waste Management Organization: Toronto, 2012.

He, H.; Shoesmith, D. W. Raman Spectroscopic Studies of Defect Structures and Phase Transitions in Hyperstoichiometric UO_{2+x}. *Phys. Chem. Chem. Phys.* **2010,** *12,* 8108–8117.

He, H.; Keech, P. G.; Broczkowski, M. E.; Noël, J. J.; Shoesmith, D. W. Characterization of the Influence of Fission Product Doping on the Anodic Reactivity of Uranium Dioxide. *Can. J. Chem.* **2007,** *85,* 702–713.

Johnson, L. H.; Ferry, C.; Poinssot, C.; Lovera, C. P. Spent Fuel Radionuclide Source Term for Assessing Spent Fuel Performance. Part 1: Assessment of the Instant Release Fraction. *J. Nucl. Mater.* **2005,** *346,* 56–65.

Johnson, L. H.; Smith, P. A. The interaction of radiolysis products and canister corrosion products and the implications for spent fuel dissolution and radionuclide transport in a repository for spent fuel. In Technical Report 00–04. Wettingen: Nagra, 2000.

King, F.; Shoesmith, D. W. Nuclear Waste Canister Materials, Corrosion Behaviour and Long-Term Performance in Geological Repository Systems. In *Geological Repository Systems for Safe Disposal of Spent Nuclear Fuels and Radioactive Waste;* Ahn, J., Apted, M. J., Eds., Woodhead Publishing Ltd: Cambridge, 2010; pp 379–420. Chapter 13.

Lucuta, P. G.; Verrall, R. A.; Matzke, Hj; Palmer, B. J. Microstructural Features of SIMFUEL—Simulated High-Burnup Nuclear Fuel. *J. Nucl. Mater.* **1991,** *178,* 48–60.

Paquette, J.; Lemire, R. J. A Description of the Chemistry of Aqueous Solutions of Uranium and Plutonium to 200°C Using Potential pH Diagrams. *Nucl. Sci. Eng.* **1981,** *79,* 26–48.

Parks, G. A.; Pohl, D. C. Hydrothermal Solubility of Uraninite. *Geochim. Cosmochim. Acta* **1988,** *52,* 863–875.

Rondinella, V. V.; Wiss, T. The High Burnup Structure in Nuclear Fuel. *Mater. Today* **2010,** *13,* 24–32.

Roudil, D.; Jegou, C.; Broudix, V.; Muzeau, B.; Peuget, S.; Deschanels, X. Gap and Grain Boundary Inventories From Pressurized Water Reactor Spent Fuel. *J. Nucl. Mater.* **2007,** *362,* 411–415.

Shoesmith, D. W. The Chemistry/Electrochemistry of Spent Nuclear Fuel as a Wasteform. In *Uranium: Cradle to Grave;* Burns, P. C., Sigmon, G. E., Eds., Mineralogical Society of Canada: Winnipeg, 2011; pp 337–368.

Shoesmith, D. W. Used Fuel and Uranium Dioxide Dissolution Studies–A Review. In *Technical Report TR-2007-03*, Nuclear Waste Management Organization: Toronto, 2007.

Shoesmith, D. W.; Kolar, M.; King, F. A Mixed Potential Model to Predict Fuel (Uranium Dioxide) Corrosion Within a Failed Nuclear Waste Container. *Corrosion* **2003,** *59,* 802–816.

Shoesmith, D. W. Fuel Corrosion Processes Under Waste Disposal Conditions. *J. Nucl. Mater.* **2000,** *282,* 1–31.

Shoesmith, D. W.; Sunder, S.; Hocking, W. H. Electrochemistry of UO_2 Nuclear Fuel. In *Electrochemistry of Novel Materials;* Lipkowski, J., Ross, P. N., Eds., VCH Publishers: New York, 1994; pp 297–337. Chapter 6.